



Full Text View

[Volume 28, Issue 2 \(February 1998\)](#)

Journal of Physical Oceanography

Article: pp. 361–388 | [Abstract](#) | [PDF \(724K\)](#)

The Dynamics of a Simple Baroclinic Model of the Wind-Driven Circulation

P. Berloff

Institute of Geophysics and Planetary Physics, University of California, Los Angeles, Los Angeles, California

S. P. Meacham

Department of Oceanography, The Florida State University, Tallahassee, Florida

(Manuscript received June 11, 1996, in final form June 26, 1997)

DOI: 10.1175/1520-0485(1998)028<0361:TDOASB>2.0.CO;2

ABSTRACT

The authors study the dynamics of a two-layer approximation to the steadily forced baroclinic circulation in a closed ocean basin with the aim of understanding its temporal variability and the onset of low-frequency variability. It is found that, for a range of dissipation that includes values used in a number of ocean modeling studies in the past five years, if one waits a sufficient length of time, the asymptotic behavior of the system is characterized by only a very small number of degrees of freedom. By varying the dissipation as a control parameter, the authors identify abrupt transitions in the form of the long-term circulation exhibited by the model. One type of transition, from a time-varying circulation dominated by two frequencies to a chaotic circulation, is accompanied by the appearance of low-frequency variability. This constitutes an internal mechanism for the production of variability at climatological timescales. The model used is a two-layer, quasigeostrophic model forced by a steady wind stress with a uniform cyclonic curl. Dissipation is modeled by a lateral diffusion of momentum with a uniform eddy viscosity. In two sets of experiments with two internal deformation radii and layer depth ratios, the eddy viscosity is varied and the types of circulation that result are reported. The stable steady circulation seen in the viscous limit gives way to time-dependent circulations of increasing temporal complexity. Spatially, the circulations fall into two types, those dominated by large recirculating gyres in the western part of the basin and those with a strong (and strongly meandering) peripheral current reminiscent of that seen in the Black Sea. From an examination of the linear eigenmodes of the steady circulation, the initial transition to time dependence may be characterized as a baroclinic instability of the western recirculation gyre.

Table of Contents:

- [Introduction](#)
- [Modeling approach and](#)
- [Results—The bifurcation](#)
- [Results: Primary instability](#)
- [Discussion and conclusions](#)
- [REFERENCES](#)
- [TABLES](#)
- [FIGURES](#)

Options:

- [Create Reference](#)
- [Email this Article](#)
- [Add to MyArchive](#)
- [Search AMS Glossary](#)

Search CrossRef for:

- [Articles Citing This Article](#)

Search Google Scholar for:

- [P. Berloff](#)
- [S. P. Meacham](#)

1. Introduction

Linear theory has long been valued for its ability to illuminate the physical mechanisms behind the onset of time dependence in physical systems. An example is the use by [Bryan \(1963\)](#) and [Ierley and Young \(1991\)](#) of the notion of the shear instability of a long western boundary current to explain the onset of time dependence in barotropic models of the wind-driven ocean circulation. In modern eddy-resolving general circulation models of the ocean circulation, the time dependence that is observed is complicated, and estimates of the effective Reynolds numbers for such flows indicate that they should be strongly nonlinear. It is the nonlinearity of the flow that is responsible for the complicated time dependence. In this paper, we explore how the baroclinic circulation in a small closed basin evolves increasingly complicated temporal variability as the level of dissipation in the model decreases. Two significant points emerge. The first is that if one waits sufficiently long for transients to die away, then for a wide range of parameters, the circulation settles down to a flow with only a small number of degrees of freedom. The associated temporal variability is then either periodic, quasiperiodic, or characterized by a “strange attractor.” The second main point is that the transition to chaotic flow is accompanied by the introduction of very low frequency variability; the wind driven circulation contains a natural, internal mechanism for producing variability at long timescales including climatological timescales. In addition, we note that parameter regimes exist in which multiple stable time-dependent circulations can be realized according to the choice of initial conditions.

The complicated time-dependent behavior of a two-layer quasigeostrophic GCM with double-gyre wind stress forcing, a free-slip boundary condition on the lateral walls, and both horizontal and bottom friction was studied by [Holland \(1978\)](#), who showed the importance of mesoscale eddies in the dynamics of the wind-driven ocean. The model circulation was in statistical equilibrium and contained a mesoscale eddy field, interacting with the time-mean flow. The circulation averaged over a large time contained an eastward jet separating the northern and southern gyres. The eddies appeared as a result of internal instabilities. Due to the high Reynolds numbers of these experiments, the instantaneous eddy fields were too complicated to be analyzed, but it was noticed that the eddies transferred energy from the upper layer to the lower. This energy transfer limited the amplitude of the upper-layer circulation and established a time-mean circulation in the lower layer.

[Ierley and Sheremet \(1995\)](#) studied a barotropic circulation in a square basin with single-gyre wind forcing and free-slip boundary conditions on the lateral walls and found multiple steady equilibria. One of the steady solutions in that case had relatively weak recirculation in the northeastern corner of the basin (anticyclonic wind stress curl was used in that study) and a well-developed western boundary intensification. Another solution was a strongly nonlinear basin-filling gyre reminiscent of a Fofonoff inertial solution ([Fofonoff 1954](#)).

A linear stability analysis ([Sheremet et al. 1997](#)) of the steady, barotropic, single-gyre circulation with no-slip conditions at the meridional walls and free-slip conditions at the latitudinal walls showed that the most unstable eigenmode of the more realistic, viscous circulation solution with weak recirculation, which appears first as the Reynolds number is increased, is trapped at the western wall. Time-dependent solutions of this problem were studied by [Kamenkovich et al. \(1995\)](#) and [Sheremet et al. \(1995\)](#). In these works, it was shown that at a critical Reynolds number, Re_1 , the trapped eigenmode becomes a growing mode and the circulation experiences an oscillatory instability that gives rise to stable periodic solutions (a Hopf bifurcation: e.g., [Drazin 1992](#)). For a range of the Reynolds numbers above this critical value, the flow is periodic, but at $Re_2 > Re_1$, another frequency appears in the time-dependent solution. At some larger Re the flow became aperiodic.

[Meacham and Berloff \(1997, hereafter MB1\)](#) examined a similar problem, that of a barotropic circulation in a rectangular basin driven by single-gyre wind forcing that differed in the use of no-slip boundary conditions. In that work, only a single family of steady states was observed. These resembled the viscous circulation solutions with weak recirculation found by [Ierley and Sheremet \(1995\)](#) but with some structural differences. In a linear stability analysis ([Meacham and Berloff 1998, manuscript submitted to *J. Mar. Res.*](#)) these solutions were found to have two modes of instability, depending on the basin aspect ratio and the strength of the forcing. One mode, prevalent in a basin with a sufficiently large meridional extent, is a western boundary current instability of the type discussed by [Ierley and Young \(1991\)](#). The second is a more complicated instability involving the inertial recirculation region and the Moore wave ([Moore 1963](#); [Pedlosky 1987](#)). [Meacham and Berloff \(1998, manuscript submitted to *J. Mar. Res.*\)](#) also observed resonances between the instabilities of the steady circulation and the normal modes of the basin.

[Cessi and Ierley \(1995\)](#) extended the results of [Ierley and Sheremet \(1995\)](#) on barotropic circulation with free-slip boundary conditions by considering double-gyre wind forcing. Cessi and Ierley showed that, for some range of parameters, the circulation possesses multiple steady states. Some of the steady states are perfectly antisymmetric solutions in which the strength of the cyclonic gyre is equal to the strength of the anticyclonic one. Other solutions appear in pairs. Each member of the pair may be obtained by applying the quasigeostrophic symmetry $y \rightarrow -y$, $\psi \rightarrow -\psi$ to the other member of the pair, but each solution is not itself invariant under this symmetry. One of the pairs corresponded to strongly nonlinear inertial recirculation gyres (one is cyclonic and another is anticyclonic), which filled the whole basin and had unrealistically large velocities.

[Jiang et al. \(1995\)](#) and [Speich et al. \(1995\)](#) found multiple steady states and periodic solutions in a double-gyre 1½-layer shallow-water model with both free-slip and no-slip boundary conditions on the lateral walls. Periodic solutions in that case arose from the steady states by Hopf bifurcations. The periodic oscillation was related to the appearance and nonlinear saturation of multipole vortices. These vortices interacted with each other and with the eastward jet that resulted from the confluence of the two western boundary currents. When the control parameter was shifted farther from the critical Hopf bifurcation value, the periodic solution became unstable and the circulation behaved aperiodically. The power spectrum of the aperiodic solution had several low-frequency spikes associated with interannual variability.

Strongly time-dependent and chaotic circulation was studied by [McCalpin and Haidvogel \(1996\)](#) in an equivalent-barotropic (reduced-gravity 1½-layer quasigeostrophic) model driven by a double-gyre wind stress (free-slip boundary conditions were used on the walls). In that case, the system had several preferred states distinguished by total energy levels and circulation patterns. Low-frequency variability in the model was associated with transitions between these preferred states. One of the states had relatively high energy with the eastward jet penetrating deeply into the interior of the basin. Meanders and rings were weak for that state and the overall circulation was characterized as quasi-stable. The low energy state had a jet with a significantly shorter zonal extent and was characterized by strong meandering and eddy formation. The state of intermediate energy was associated with a modest generation of meanders and eddies. In that case, the extent of the eastward jet was shorter than in the high energy state but longer than in the low energy state.

Recently, the works of MB1 and [Berloff and Meacham \(1997\)](#), hereafter BM1) contributed to the study of the wind-driven circulation by finding a variety of the low-dimensional attractors of the flow, that is, stable but, in general, time-dependent circulation patterns with a temporal variability that could be characterized by only a few active degrees of freedom. In MB1 the circulation model was barotropic; in BM1 it was equivalent-barotropic. Both models used single-gyre wind stress forcing and no-slip boundary conditions. In BM1 and MB1, the models were thought of as large-dimensional forced and dissipative dynamical systems. The attractors of such systems are important in determining the intrinsic timescales and spatial patterns of the time-dependent flow. In addition to a single branch of steady-state circulations (fixed points), a rich structure of more complicated, low-dimensional, large-time asymptotic attractors was found for a wide range of the control parameters. When viewed in phase space, these attractors included limit cycles, tori, and fractal (chaotic) attractors. A limit cycle corresponds to a periodic oscillation of the flow. Tori yield either quasiperiodic oscillations with two or three dominant frequencies or phase-locked periodic orbits ([Drazin 1992](#)). A fractal attractor is associated with deterministically chaotic behavior of the flow. For some ranges of the control parameters, multiple stable attractors coexist. The bifurcations leading from one attractor to another, as the parameters are varied, were found to be either Hopf or period-doubling bifurcations. In MB1 and BM1 it was found that the dimension of the chaotic attractors grows slowly as Re is increased [the way in which the structure of the attractors change in the “chaotic regime” is quite complicated with islands of periodicity, and quasiperiodicity reminiscent of the behavior of one-dimensional maps, e.g., [Collet and Eckmann \(1980\)](#)]. Some frequencies associated with motion on the low-dimensional attractors corresponded to variability on timescales ranging from centennial to interannual. In the chaotic regimes, the power spectrum of variability became increasingly red as the supercriticality was increased; thus much of the variability in the most energetic flows was associated with timescales greater than 1 yr.

The results of [Jiang et al. \(1995\)](#), [Speich et al. \(1995\)](#), MB1, and BM1 suggest that for some control parameter ranges, including those widely used in modern GCMs, discrete numerical models with a very large number of degrees of freedom may behave as relatively simple nonlinear oscillators. Such oscillators are achieved asymptotically in a large-time limit and are associated with motion on low-dimensional topological objects in phase space. Convergence to the oscillator physically corresponds to a significant self-organization of the flow. The oscillations associated with the motion on the attractors are achieved with no variations in the external forcing. This *natural* variability of the GCMs and, presumably of the real ocean, should not be neglected in ocean modeling efforts. The low-frequency part of the natural variability spectrum may be very important for climatic studies and long-term predictions.

In this work we extend the previous results of MB1 and BM1 to a baroclinic model of the wind-driven single-gyre circulation and explore how the presence of baroclinicity changes the successive bifurcations and the structure of the low-dimensional attractors if compared to the barotropic (MB1) and equivalent-barotropic (BM1) models. The simplest baroclinic model with two layers is a proper link in a hierarchy of models extending from the simpler two-dimensional (2D) barotropic and equivalent-barotropic representations to fully three-dimensional (3D) and, therefore, more realistic models of the wind-driven circulation in the ocean. We note that [Quon and Ghil \(1995\)](#) found stable nonlinear oscillations and successive bifurcations between different attractors in a 2D thermohaline circulation problem. The results of the various works cited, as well as our present baroclinic study, suggest that low-dimensional behavior in numerical circulation models is a robust feature. We conjecture that the presence of an underlying low-dimensional dynamics in more sophisticated models, which include topography, heat and freshwater fluxes, as well as wind stress forcing, is possible and indeed likely, though the effective dimension will probably be larger than three or four. It is unclear what the role of semidiscrete processes such as “convective adjustment” will be in such models.

The results of this paper are relevant to the wind-driven circulation in a midlatitude ocean, but in choosing the size of our basin, the stratification, and the specific wind forcing, we were guided by the sizes and hydrology of the Black Sea. A discussion of the structure of the Black Sea circulation is contained in [Stanev \(1990\)](#). The Black Sea exhibits a recurrent

large-scale organization of the flow into two dominant basin filling cyclonic cells, referred to in the literature as the Eastern and Western Gyres ([Oguz et al. 1993](#)).

Another organized feature is the cyclonic Rim Current ([Oguz et al. 1993](#)) flowing around the periphery of the basin. The Rim Current is a relatively narrow jet above the permanent pycnocline. It has a typical width of about 75 km and velocities of about $0.2\text{--}0.3\text{ m s}^{-1}$ at the surface and exhibits strong meandering. The Rim Current separates the gyres from a series of baroclinic eddies confined near the coast. The eddies are anticyclonic above and cyclonic below the permanent pycnocline. At a depth of 500–1000 m, observations ([Filippov 1961](#)) helped to identify countercurrents flowing along the shelf break and under the surface Rim Current. A mechanism, supporting both the Rim Current and countercurrents, is not known at present. Whereas these features may be strongly influenced by the continental slope topography, some insight into the nature of the rim current can be gained from the flat-bottom model used in this paper. The large-scale organization of the flow in the Black Sea may be an indication of an underlying low-dimensional dynamics guiding the complicated behavior of the flow. In this paper, we are interested in identifying the low-dimensional attractors of our simplified model and in characterizing the spatial and temporal organization of the flows that are associated with them.

The quasigeostrophic potential vorticity equations for the upper and lower layer, which we solve numerically, are a pair of forced and dissipative partial differential equations. The theory of several classes of such systems is discussed in [Robinson \(1995\)](#), [Temam \(1995\)](#), and [Lions et al. \(1992\)](#). Also relevant is work demonstrating the existence of inertial manifolds (e.g., [Constantin et al. 1989](#)). The rather technical mathematical results contained in these works, in effect, say that one should expect such systems, which are formally infinite dimensional, to exhibit finite dimensional attractors. Moreover, in sufficiently dissipative systems, the dimension of these attractors should be small. In order to model these equations numerically, we discretize the PDEs in a standard way (cf. [Holland 1978](#)). This produces a system of many discrete ordinary differential equations coupled through nonlinearity. We then look for attractors of relatively low dimension (about three or less) at sufficiently small Reynolds numbers.

2. Modeling approach and methods

Our numerical calculations are based on a two-layer, quasigeostrophic β -plane model ([Phillips 1954](#); [Pedlosky 1987](#)).

We modeled the circulation in a rectangular basin with a zonal extent, $L_x = 800\text{ km}$, and meridional extent, $L_y = 400\text{ km}$. The Coriolis parameter is $f = f_0 + \beta_0 y$, where $f_0 = .93 \times 10^{-4}\text{ s}^{-1}$, $\beta_0 = 2 \times 10^{-11}\text{ m}^{-1}\text{ s}^{-1}$. Vertical stratification was modeled by two layers with finite depths, one layer above and another below the permanent thermocline. The depths at rest were H_1 for the upper and H_2 for the lower layer. The total depth $H = H_1 + H_2 = 2\text{ km}$ was fixed in our experiments. The densities were ρ_1 and ρ_2 for the upper and lower layers respectively. The reduced gravitational acceleration was

$$g' = \frac{\rho_2 - \rho_1}{\rho_1} g = 2.575 \times 10^{-2}\text{ m s}^{-2}.$$

The model did not include explicit vertical friction, and the layers communicated only through pressure forces. Horizontal momentum diffusion was parameterized in the vorticity equation in the form of $\nu \nabla^4 \psi_{1,2}$ with a uniform eddy diffusivity ν (ψ_1, ψ_2 were the upper and lower layer streamfunctions, respectively). No bottom topography and bottom drag were included in the model. The boundary conditions on the lateral walls were no-slip and no-normal flow. On the upper surface we used a rigid-lid approximation. The upper layer was forced by a steady wind stress treated as a body force acting on the upper layer. The wind stress τ had a uniform, cyclonic curl of τ_0/L_x . In all experiments, τ_0 was fixed at 0.5 dyn cm^{-2} . All the parameters used in this study are listed in [Table 1](#).

The choice of basin size, β_0 , wind forcing, boundary conditions, and momentum diffusion formulation are the same as those used in BM1, but instead of the infinitely deep lower layer, as required by the $1\frac{1}{2}$ -layer formulation in BM1, we used a model with a finite lower-layer depth. This two-layer formulation allows baroclinic instability in the model, while a vertical resolution of only two layers allows the extensive computations required in a study of the low-dimensional attractors of the system for a wide range of parameters.

We used the following nondimensionalization of the two-layer quasigeostrophic equations: L_x for the length scale, $(\beta_0 L_x)^{-1}$ for the timescale, τ_0 for the wind stress scale, and $H_{1,2}$ for the depth scales of the layers. The upper-layer Sverdrup balance yielded the velocity scale $U = \tau_0(\rho H_1 L_x \beta_0)^{-1}$. One can define several auxiliary horizontal length scales:

$$R_d = \frac{\sqrt{g'}}{f_0} \sqrt{\frac{H_1 H_2}{H_1 + H_2}};$$

$$\delta_I = \sqrt{\frac{U}{\beta_0}}; \quad \delta_M = \left(\frac{\nu}{\beta_0}\right)^{1/3}.$$

Here δ_I and δ_M are the inertial and viscous length scales, respectively, and R_d is the baroclinic deformation radius. The nondimensionalization of the problem yielded five nondimensional parameters:

$$\delta = \frac{L_y}{L_x}; \quad \epsilon = \left(\frac{\delta_I}{L_x}\right)^2; \quad \mu = \left(\frac{\delta_M}{L_x}\right)^3;$$

$$S = \left(\frac{L_x}{R_d}\right)^2; \quad \gamma = \frac{H_1}{H_2}. \quad (1)$$

When compared to the 1½-layer formulation of BM1, a new parameter, γ , appears. After invoking the quasigeostrophic approximation, the nondimensional potential vorticity equations are

$$\frac{\partial \zeta_1}{\partial t} + \epsilon J(\psi_1, \zeta_1) + \frac{\partial \psi_1}{\partial x} = \nabla \times \tau + \mu \nabla^4 \psi_1$$

$$\frac{\partial \zeta_2}{\partial t} + \epsilon J(\psi_2, \zeta_2) + \frac{\partial \psi_2}{\partial x} = \mu \nabla^4 \psi_2, \quad (2)$$

where the perturbation potential vorticities of the upper and lower layers $\zeta_{1,2}$ are connected with the corresponding streamfunctions through the coupled elliptic equations:

$$\left(\nabla^2 - \frac{S}{1 + \gamma}\right) \psi_1 + \frac{S}{1 + \gamma} \psi_2 = \zeta_1$$

$$\left(\nabla^2 - \frac{S\gamma}{1 + \gamma}\right) \psi_2 + \frac{S\gamma}{1 + \gamma} \psi_1 = \zeta_2. \quad (3)$$

Here, the perturbation potential vorticity is defined as the full, quasigeostrophic layer potential vorticity minus the planetary vorticity. Since we will never refer to the full potential vorticity, we shall subsequently refer to the perturbation potential vorticity simply as the potential vorticity. Introducing barotropic and baroclinic streamfunctions, ψ_{BT} and ψ_{BC} , defined as

$$\psi_{\text{BT}} = \frac{S\gamma}{1 + \gamma} \psi_1 + \frac{S}{1 + \gamma} \psi_2, \quad \psi_{\text{BC}} = \psi_1 - \psi_2, \quad (4)$$

the elliptic problem (3) can be diagonalized as

$$\nabla^2 \psi_{\text{BT}} = \frac{S\gamma}{1 + \gamma} \zeta_1 + \frac{S}{1 + \gamma} \zeta_2$$

$$(\nabla^2 - S) \psi_{\text{BC}} = \zeta_1 - \zeta_2. \quad (5)$$

The boundary conditions were no-normal flow through the lateral boundaries:

$$\psi_{1,2}|_C = \Gamma_{1,2}(t), \quad (6)$$

and no-slip at the lateral boundaries:

$$\left. \frac{\partial \psi_{1,2}}{\partial n} \right|_C = 0. \quad (7)$$

These are supplemented by the mass conservation constraint for each layer:

$$\frac{\partial}{\partial t} \iint_A \psi_{1,2}(x, y) dx dy = 0. \quad (8)$$

In (7), (8) C is the basin's bounding contour and A is the basin's area.

Equations (2) and (5) in dimensional form were discretized using second-order finite differences on a 129×65 equally spaced grid (6.25-km resolution) and solved numerically using boundary conditions (6), (7), and the mass conservation law (8). Here we followed the procedure outlined in BM1 for the equivalent-barotropic model. Except for the particular method used to solve the elliptic problems (5), and the choice of boundary conditions, the method is similar to that used by Holland (1978).

Some of the more time-dependent flows that we will examine look quite complicated when viewed in physical space with mesoscale eddies and strongly meandering boundary currents. This can obscure the fact that the time dependence is relatively straightforward. There are several ways of focusing on the time dependence of the flows. The two main ones that we shall use are the examination of power spectra and an approach borrowed from the theory of dynamical systems. The equations that we solve may be viewed as an autonomous dynamical system of large dimension p . The states $\mathbf{x}(t)$ of the system are p -dimensional phase space vectors with coordinates $\psi_{1,2,i}$, that is, the values of the streamfunctions at each of the nodes of the computational grid (i is the index of a node in the basin). This dynamical system is controlled by the set of parameters $\mathbf{a} = (\delta, \epsilon, \mu, S, \gamma)$ and can be formally written as

$$\dot{\mathbf{x}} = \mathbf{F}(\mathbf{x}; \mathbf{a}), (9)$$

where $\mathbf{F}(\mathbf{x}; \mathbf{a})$ is a nonlinear operator acting on the vector $\mathbf{x}(t)$. Starting from an arbitrarily chosen initial state, the time-dependent behavior of the circulation in the basin is uniquely described by the trajectory $\mathbf{x}(t)$ in the p -dimensional phase space. The dynamical system that we explore is dissipative. For a dissipative system, we expect that the trajectories will converge onto sets of dimension lower than p . In physical space, this behavior will correspond to some degree of self-organization of the flow. As an example, if trajectories in phase space converge to an attractor that is a simple closed curve, then, after a sufficient time that initial transients have died away, the circulation will evolve periodically. In particular, a time series of ψ at every grid point will be periodic with the same period. The dimension of the attractor provides an indication of the number of degrees of freedom in the flow, though it is not synonymous with the number of degrees of freedom. Generally, the temporal behavior on a smooth m -dimensional attractor can be modeled with a set of n ODEs for some $n \leq 2m + 1$. We are interested in identifying attractors with dimension a priori less than 4. The main reason for this is that it is technically difficult to identify attractors of larger dimension. For example, the amount of data required to reliably estimate the dimension of an attractor increases exponentially with the dimension. Empirically, the transition to chaos in ocean models of this type appears to occur from attractors with dimensions of either 2 or 3. (This behavior is also to be anticipated on theoretical grounds.)

To look at low-dimensional attractors, we do not need to examine the whole p -dimensional phase space; instead low-dimensional projections of the full phase space will suffice. Imagine bending a wire into a closed, continuous curve but one that is warped so that it does not lie in a plane. The wire curve exists in three dimensions, but if it is placed in a beam of light and its shadow is projected on a two-dimensional screen, the shadow is, in general, still recognizable as a closed curve (though it may intersect itself).

There are a number of ways of constructing low-dimensional projections. The technique used here is a method that has been used successfully in several studies of chaotic flows in the laboratory. We first started the model from some initial state, advanced it in time, and recorded the time series of the basin integrated total energy of the flow. The nondimensional energy density of the the system (Pedlosky 1987) is

$$E(x, y, t) = \sum_{i=1,2} \frac{H_i}{H} \frac{|\nabla \psi_i|^2}{2} + \frac{S\gamma}{2(1+\gamma)^2} (\psi_2 - \psi_1)^2, \quad (10)$$

where the sum is the kinetic energy and the last term is the available potential energy. From the energy time series, we constructed low-dimensional phase space projections using the *method of delay coordinates* (Packard et al. 1980; Takens

1981; Broomhead and King 1986), in which coordinates x_0, x_1, \dots, x_N in an artificial phase space are generated from copies of the original (energy) time series successively delayed by Φ ; that is,

$$x_j(t) = \frac{1}{A} \iint_A E(x, y, t - j\phi) dx dy.$$

For a discussion of this method and the choice of the fixed time delay Φ and dimension N , see the previous two references or MB1 and BM1. Examples of the use of the method of delay coordinates in studies of laboratory experiments can be found in Pfister et al. (1992) and Brandstater and Swinney (1987). Applications to numerical wind-driven circulation problems may be seen in MB1 and BM1.

Instead of the energy time series, one, in principle, could choose time series of any time-dependent variable of the system. The choice of time series changes the choice of projection from the full phase space to the reduced phase space but does not change the nature of the underlying attractor; that is a function of the dynamics alone. The shape of the attractor will be distorted compared to the energy time series projection, but its topology, in which we are mainly interested, will not change except for possible changes in the number of self-intersections. In the example given above of the wire in the projector beam, we can imagine rotating the wire curve or warping the screen. The shape of the projected image will change but, in general, it will still remain recognizable as a closed curve. This remains true for strange attractors if the chaos in the system is only temporal but, if the chaos becomes spatiotemporal, this is not the case. In some preliminary experiments with a wind-driven barotropic model, we found that, for the Reynolds numbers significantly higher than those used in this study, chaotic behavior remains spatially correlated in the large-time limit.

We integrated the model in time until the corresponding phase space trajectory converged to some low-dimensional attractor. This procedure enabled us to find such attractors as fixed points, limit cycles, tori, and strange attractors. A fixed point corresponds to a steady-state circulation; a limit cycle yields an oscillation of the flow with one distinctive frequency. Motion on a torus in phase space may correspond either to quasiperiodic oscillations with two distinctive frequencies, or to a phase-locked trajectory, which is associated with a purely periodic oscillation (though the trajectory still winds around the torus). Since it is difficult to empirically differentiate truly quasiperiodic orbits and phase-locked trajectories of very long period, we will refer to either of these types of motion somewhat inaccurately as quasiperiodic. Motion on a strange attractor corresponds to chaotic behavior of the flow.

In order to find the most unstable eigenmode of the primary bifurcation we followed the procedure described in BM1. For the attractor dimension measurement we used the *nearest neighbor algorithm* (Badii and Politii 1985) implemented in the software of Kostelich (1990). For reasons stated earlier, we did not attempt to apply this algorithm for an attractors with a dimension greater than four because this would require an impractical amount of computer resources.

3. Results—The bifurcation sequences

In this section, we will see how the time-dependence of the flow changes as we increase the Reynolds number (by decreasing the viscosity) in two sets of experiments with differing deformation radii. Because of the small meridional extent of the basin, the instability that initially gives rise to time dependence will be seen (in section 4) to be an instability of the main recirculation gyre rather than a western boundary current instability. Several transitions, relatively closely spaced in ν (or μ), will be seen to lead to chaotic flow, but, as the viscosity is decreased further, the chaotic flow will give way to quasiperiodic and periodic behavior as a resulting of an increasing barotropization of the flow by eddy processes. For a broad range of viscosities (down to approximately $100 \text{ m}^2 \text{ s}^{-1}$ in the case of the smallest deformation radius used), the flow will be found to asymptote to a low-dimensional attractor. At small viscosities, the flow once again becomes chaotic. The transition to chaos is accompanied by the appearance of low-frequency variability. When the deformation radius is sufficiently small and the upper layer is shallow, the strongly nonlinear flow qualitatively resembles the flow seen in the Black Sea during the summer months with a strong peripheral current and many mesoscale eddies.

We carried out two sets of experiments. Our parameter choices are motivated by the Black Sea but have been idealized to suit the more process-oriented nature of this study. In each set, we kept the total depth H and g' fixed but changed the depth ratio $\gamma = H_1/H_2$. Stanev (1990) showed that the circulation in the Black Sea can be well approximated by a two-layer model with the upper layer about 10–20 times thinner than the lower layer one. Therefore, in the first set we fix $\gamma = 1/9$, and in the second set we fix $\gamma = 1/19$. In terms of layer depths we used $H_1 = 200 \text{ m}$, $H_2 = 1800 \text{ m}$ (in the first set) or $H_1 = 100 \text{ m}$, $H_2 = 1900 \text{ m}$ (in the second set). The internal Rossby deformation radius in the Black Sea is estimated to be 20–25 km (Oguz et al. 1992). In the first set of experiments we keep the deformation radius in this range, but in the second set, we use a slightly shorter $R_d = 16.813 \text{ km}$ in order to emphasize the dependence of the circulation on R_d . Some Russian colleagues have argued that the deformation radius may be less than 20 km in parts of the Black Sea. Of the nondimensional

parameters, S and ϵ differ between the two sets. In the first set $S = 1194.4$ ($R_d = 23.148$ km), $\epsilon = 1.22 \times 10^{-3}$; in the second set $S = 2264.0$ ($R_d = 16.813$ km) and $\epsilon = 2.44 \times 10^{-3}$; thus, in the second set of runs, the baroclinic deformation radius is smaller by a factor 0.73 and, for a given value of viscosity, the upper-layer flow is more nonlinear. The only variable parameter within each set of experiments was the viscosity coefficient ν , or μ in terms of the nondimensional parameters.

a. The location of the initial instability

For sufficiently high ν , we found steady states (or fixed points in phase space) with no flow in the lower layer. Since we started the time integration from a state of rest, the circulation experienced an adjustment. During the adjustment, perturbations in the lower layer grow initially, then decay, and the system tends toward a steady state. The steady states coincide with the steady states of the equivalent-barotropic and barotropic models discussed in BM1 and MB1. The sequence of steady states for different ν is shown in [Fig. 1](#) (from BM1). The baroclinic steady solutions, the equivalent-barotropic and barotropic solutions all differ in their stability properties. For the depth ratio $\gamma = 1/9$ and $R_d = 23.148$ km, the baroclinic steady state suffered an oscillatory instability at a critical value of ν , ν_c , say, lying between 222 and 223 $\text{m}^2 \text{s}^{-1}$. At this value of ν , a periodically oscillating solution (limit cycle) is generated via a Hopf bifurcation. The Hopf bifurcation in this case is supercritical so that just below ν_c we see a family of *stable* limit cycles with amplitude that increases like $(\nu_c - \nu)^{1/2}$. (All Hopf bifurcations found in this study are supercritical to a local accuracy equal to the distance between the neighboring values of ν for which the experiments were performed.) For $\gamma = 1/9$ and $R_d = 16.813$ km, the stability threshold was higher: 550 $\text{m}^2 \text{s}^{-1} < \nu_c < 560$ $\text{m}^2 \text{s}^{-1}$. In the first set of experiments, the Reynolds number is defined as $\text{Re} = UL_x/\nu$ is $56.3 > \text{Re}_{\text{crit}} > 56.05$ at the primary bifurcation, and in the second set $45.45 > \text{Re}_{\text{crit}} > 44.64$.

We compared the critical values of ν corresponding to the primary instability in the two-layer quasigeostrophic and the equivalent-barotropic models. In the equivalent-barotropic model studied by BM1, the deformation radius was $R_d = 24.4$ km. To make the comparison, we used the same values of R_d , δ , and ϵ in the two-layer model and chose the depth ratio $\gamma = 1/9$. In the equivalent-barotropic model, due to the presence of the infinitely deep lower layer, $\gamma = 0$. We found that the primary Hopf bifurcation in the two-layer model with these parameters occurred at $\nu \approx 205$ $\text{m}^2 \text{s}^{-1}$ ($\text{Re}_{\text{crit}} \approx 60.98$). This value is significantly higher than the critical value $\nu \approx 104$ $\text{m}^2 \text{s}^{-1}$ ($\text{Re}_{\text{crit}} \approx 120.19$) reported in BM1 for the equivalent-barotropic circulation. This result indicates that the baroclinic flow is less stable than the equivalent-barotropic flow with fixed R_d , δ , and ϵ . The presence of the active lower layer with finite depth ($\gamma \neq 0$) destabilized the flow.

This difference between stability thresholds of the 1/2- and two-layer models comes from the fundamentally different physical mechanisms responsible for the primary Hopf bifurcation. In the two-layer model, the primary instability is a baroclinic instability of part of the western gyre, whereas in the 1/2-layer case (BM1) it was a complex barotropic instability involving the western boundary intensification, the western recirculation, and the meander between the western and the central gyres, denoted **A**, **B**, and **C** respectively in the last panel of [Fig. 1](#). An analysis of the instability responsible for the transitions from steady to unsteady circulations is contained in [section 4](#).

In principle, other steady-state branches may exist. Multiple steady states were found by [Ierley and Sheremet \(1995\)](#) and [Cessi and Ierley \(1995\)](#) for the case of free-slip boundary conditions with single-gyre and double-gyre wind forcing. For the case of no-slip boundary conditions, [Speich et al. \(1995\)](#) showed that multiple steady states exist when a double-gyre wind forcing is used. Here we use no-slip boundary conditions and single-gyre wind forcing. We did not discover multiple branches of steady solutions, but the search for additional steady-state branches was not exhaustive.

b. Depth ratio $\gamma = 1/9$; $R_d = 23.148$ km

In this set of experiments, the parameter ν was varied over the range from 140 to 260 $\text{m}^2 \text{s}^{-1}$.

We define the mean energy as an arithmetic mean between the highest and the lowest values of the energy achieved on the attractor and the amplitude of a time-dependent solution as the difference between the highest and lowest values of energy. An empirical bifurcation diagram, which helps to locate transitions in solution structure in parameter space, is shown in [Fig. 2](#). In this figure, we plotted the total energy amplitude as a percentage of the mean energy. In [Fig. 3](#), we show a bifurcation diagram in terms of the mean energy. The notion that the mean energy of the circulation decreases with increasing Reynolds number over a sizable range of Reynolds numbers at first may seem counterintuitive. The kinetic and potential parts of the total energy are shown in [Fig. 4](#), and it is clear that the decrease of the total energy with decreasing

ν that is seen for values of ν less than $170 \text{ m}^2 \text{ s}^{-1}$ is mainly associated with the decrease of potential energy. Potential energy decreases because the flow becomes more barotropic for the lower values of ν . This is consistent with the energy cascade ideas of [Rhines \(1977\)](#) since as ν decreases we see a considerable amount of mesoscale variability produced by baroclinic instability.

The primary Hopf bifurcation occurs for a value of the viscosity coefficient ν between 222 and $223 \text{ m}^2 \text{ s}^{-1}$. A limit cycle arises as a result of this bifurcation and grows in amplitude as ν is reduced further. Let us define the time-averaged streamfunctions as

$$\langle \psi_i \rangle(x, y) = \frac{1}{T} \int_{t_0}^{t_0+T} \psi_i(x, y, t) dt, \quad i = 1, 2, \quad (11)$$

where T is the limit cycle period, if the formula is applied to a limit cycle; for other attractors, T is a large value chosen empirically. The perturbation streamfunctions are defined as

$$\psi'_i(x, y, t) = \psi_i(x, y, t) - \langle \psi_i \rangle(x, y), \quad i = 1, 2. \quad (12)$$

The spatiotemporal structure of the perturbation streamfunctions on the limit cycle at $\nu = 220 \text{ m}^2 \text{ s}^{-1}$ (not shown) is similar to the structure of the most unstable eigenmode of the unstable steady circulation at $\nu = 220 \text{ m}^2 \text{ s}^{-1}$ (see [Figs. 16a](#) and [b](#) and the discussion of the eigenmode energetics in [section 4](#)). The period of the limit cycle at $\nu = 220 \text{ m}^2 \text{ s}^{-1}$ was 119 days; the period of the eigenmode was 118.7 days. These similarities suggest that the oscillation on the limit cycle is a nonlinearly saturated modification of the eigenmode. The period of the limit cycle changes gradually from 119.5 to 112.5 days as ν is reduced.

The limit cycle loses stability as a result of a secondary Hopf bifurcation at ν between 185 and $187 \text{ m}^2 \text{ s}^{-1}$, and the system yields a stable toroidal attractor around which trajectories wind, giving rise to quasiperiodic motion or a phase-locked periodic trajectory. Since our techniques fail to distinguish between a truly quasiperiodic trajectory and a trajectory with period longer than the time series record, we use the term quasiperiodic for both truly quasiperiodic and long-period trajectories *on a torus*. This quasiperiodic motion contains two dominant frequencies; the new frequency associated with the secondary bifurcation is $\omega_1 = 0.006 \dots \text{ rad/day}$ (1050 days). The toroidal attractor appears to lose stability and give way to a chaotic attractor at a value of ν between 171 and $172 \text{ m}^2 \text{ s}^{-1}$.

Motion on chaotic attractors can be recognized and distinguished from trajectories on tori by means of power spectra and Poincaré sections. The spectrum of a quasiperiodic trajectory typically has 2 (for a 2-torus) or 3 (for a 3-torus) distinctive spikes with incommensurate frequencies together with additional spikes corresponding to harmonics and cross-harmonics. The spectrum of a chaotic trajectory typically has some broadband structure. The Poincaré section of a quasiperiodic trajectory on a 2-torus consists of points lying on a curve (or set of curves). A chaotic trajectory yields a Poincaré section with points covering some fractal set on the plane. In [Fig. 5](#), we show the delay coordinate phase space projection of the quasiperiodic trajectory at $\nu = 178 \text{ m}^2 \text{ s}^{-1}$, its Poincaré section, and its power spectrum. In [Fig. 6](#), we show the delay coordinate phase space projection, Poincaré section, and the spectrum of the chaotic trajectory at $\nu = 171 \text{ m}^2 \text{ s}^{-1}$. Provided that the time series is sufficiently long, one can estimate the information dimension of the attractor. A chaotic attractor will normally yield a fractional dimension. This latter technique is computationally expensive and, as will be seen further in the text, we applied it only to two chaotic attractors, one for each set of experiments.

The bifurcation associated with the transition between the attractors at $\nu = 172$ and $\nu = 171 \text{ m}^2 \text{ s}^{-1}$ appears to involve a Hopf bifurcation because the spectrum of the chaotic attractor at $\nu = 171 \text{ m}^2 \text{ s}^{-1}$ has a new spike with $\omega = 0.013 \dots \text{ rad/day}$ (a period of 480 days) as shown in [Fig. 6](#). The toroidal attractor reappears at $\nu = 170 \text{ m}^2 \text{ s}^{-1}$ as a result of a phase locking between the $0.0065 \dots$ and $0.013 \dots \text{ rad/day}$ components, but at $\nu = 169 \text{ m}^2 \text{ s}^{-1}$ the attractor is again chaotic. This is typical behavior in a regime characterized by low-dimensional behavior.

According to the results of [Newhouse et al. \(1978\)](#), which are based, in turn, on the results of [Ruelle and Takens \(1971\)](#), the 3-torus (torus with three incommensurate frequencies) that appears after three successive Hopf bifurcations in a system is structurally unstable. A stable chaotic (or strange) attractor lying on a 3-torus may appear in that case. A transition to chaos in systems with three incommensurate frequencies has been found repeatedly (cf. [Gollub and Benson 1980](#)), but it is still not clear if a typical chaotic attractor appearing at the onset of chaos lies on the 3-torus or not. [Battelino et al. \(1989\)](#) and [Giberti and Zanasi \(1993\)](#) explored systems in which transition from a 3-torus to chaos was associated with the breakup of a 3-torus. The resulting chaotic attractor did not lie on the torus in that case. Transitions on and from a 2-torus can also

lead to chaotic motion. One possible route to chaos on a 2-torus comes from the overlapping of the resonance bands associated with mode-locking on the torus (Bak et al. 1985). There are several physical examples of this behavior including laboratory results from a Rayleigh–Benard convection experiment (Fein et al. 1985). The breakup and disappearance of a 2-torus is also a possible scenario for the transition to chaos and was studied by Franceschini and Tebaldi (1984), but we have not found evidence of a similar transition in our ocean model. Franceschini and Tebaldi showed that the collision of a torus with an unstable periodic orbit may destroy the torus in a global bifurcation. The appearance of a strange attractor in that case occurs when the torus is in the vicinity of the unstable orbit. The breakup of the torus is associated with the formation of folds on its surface. It is hard to describe properly the nature of the transition from motion on tori to chaos in our present study because this would require very extensive computations at the parameter values in the vicinity of the onset of chaos for which we do not have the computational resources. Also, we are not able to distinguish homoclinic bifurcations, which involve collision of a torus with an unstable invariant set such as a fixed point, limit cycle, or another torus. Our techniques are not designed to find unstable invariant sets with the exception of unstable fixed points.

The power spectrum of the chaotic attractor at $\nu = 167 \text{ m}^2 \text{ s}^{-1}$ is shown in Fig. 7. This spectrum shows a concentration of power at low frequencies that is typical for the chaotic attractors of the present problem. Note that significant power is present at a decadal timescale. The red character of the power spectrum increases still further for chaotic motion at lower values of ν . Chaotic attractors found in MB1 and BM1 also exhibited high power at low frequencies and, therefore, low-frequency variability. In the barotropic case, for which very long runs could be made, significant variability was found at centennial timescales. The present baroclinic study suggests that this variability may be a robust feature of the wind-driven circulation in a chaotic regime. While there are many other potential sources of variability at climatological timescales, it is interesting that the nonlinearity in the dynamics of the wind-driven circulation is sufficient to generate such variability.

As the bifurcation diagram in Fig. 2 shows, in the range of ν below the critical secondary Hopf bifurcation value, the only stable attractors that we found were tori and strange attractors. In Fig. 3, we plot the mean energies of the attractors versus ν . The tori with quasiperiodic motion on them are organized in four branches, denoted in Figs. 2 and 3 by I, Ia, II, and III. Each torus has two distinctive frequencies associated with motion on it. One of those frequencies is a continuation of the original limit cycle frequency, and we traced its presence through all successive attractors. We denote this frequency by ω_0 . The value of ω_0 gradually decreases from 0.053 . . . rad/day (a period of 119.5 days) at the primary bifurcation down to 0.063 . . . rad/day (a period of 100 days) at $\nu = 140 \text{ m}^2 \text{ s}^{-1}$. The values of the second dominant frequency are different on all branches. Along branch I, the second frequency is about $\omega_1 = 0.006$. . . rad/day (a period of 1050 days). A similar value of the second frequency characterizes branch Ia: $\omega_{1a} = 0.0065$. . . rad/day (a period of 970 days). It is possible that branch Ia is a continuation of branch I and that there is a family of unstable tori connecting the stable fragments I and Ia. The second frequency at branch II is $\omega_2 = 0.004$. . . rad/day (a period of 1570 days), and at branch III it is $\omega_3 = 0.013$. . . rad/day (a period of 480 days).

At $\nu = 148 \text{ m}^2 \text{ s}^{-1}$ we found two attractors. The attractor with the higher amplitude was chaotic and the attractor with the lower amplitude belonged to branch III of tori. When we used a point on a trajectory on the chaotic attractor of case $\nu = 148 \text{ m}^2 \text{ s}^{-1}$ as an initial condition for a run with $\nu = 147 \text{ m}^2 \text{ s}^{-1}$, the trajectory was attracted to a torus on branch III, which suggests that branch Ia became unstable. When we used the trajectory on the toroidal attractor at $\nu = 148 \text{ m}^2 \text{ s}^{-1}$ (branch III) as an initial condition and fixed ν at $149 \text{ m}^2 \text{ s}^{-1}$ the trajectory converged to a torus on branch Ia. This suggests that branch III became unstable at a value of ν between 148 and $149 \text{ m}^2 \text{ s}^{-1}$. That the second frequencies on branches Ia and III are rather different suggests that the branches may not be continuations of each other. Given the finite length of these runs it is not possible to unambiguously identify the point at which the solutions on branch Ia lose stability. It is possible that the solution seen at $\nu = 148 \text{ m}^2 \text{ s}^{-1}$ that appears to continue branch Ia may be a chaotic transient of very long duration.

We have estimated the information dimension (see discussion of this dimension in Farmer et al. 1983) of the chaotic attractor at $\nu = 145 \text{ m}^2 \text{ s}^{-1}$. For this purpose we computed a total energy time series of 10^5 points (each one is one day apart), estimated the dimension, then extended the record up to 1.5×10^5 points and obtained a second estimate. Both estimates lay between 3.45 and 3.49.

In this set of experiments, the circulation contained a distinctive pair of recirculation gyres for all values of ν . For the time-dependent regimes, we always observed gyres in both the time-averaged and the instantaneous patterns of the flow, although the gyres in the instantaneous streamfunction fields are always distorted by the fluctuations of the flow. In Fig. 8, we show snapshots of ψ_1 and ψ_2 on the chaotic attractor at $\nu = 140 \text{ m}^2 \text{ s}^{-1}$. The two main upper-layer recirculation gyres are well developed. A third, eastern recirculation has a rather small amplitude, although it exists in the time-mean for the lowest values of ν in this set of experiments. It is possible that the pair of gyres in the upper layer is analogous to the

Western and Eastern Gyres of the Black Sea (Oguz et al. 1993). A similar pair of strong gyres was observed in the barotropic model of MB1 and in the EB circulation of BM1 in both the steady and time-dependent regimes. These gyres are a robust feature of the model in the parameter ranges explored.

c. Depth ratio $\gamma = 1/19$; $R_d = 16.813$ km

In this second set of experiments, the viscosity coefficient ν was varied from 100 to 580 $\text{m}^2 \text{s}^{-1}$ and the resulting bifurcation sequence is shown in Figs. 9 and 10. The steady circulation lost stability at a critical value of ν between 550 and 555 $\text{m}^2 \text{s}^{-1}$ as a result of a Hopf bifurcation. The period of the most unstable eigenmode at $\nu = 550 \text{ m}^2 \text{ s}^{-1}$ was about 92 days. The limit cycle appearing at the supercritical values of ν increases in amplitude as ν is decreased. The frequency that appeared at the primary bifurcation gradually decreases from 0.068 . . . to 0.057 . . . rad/day (the period increases from 92 to 110 days) as ν changes from 555 to 112 $\text{m}^2 \text{s}^{-1}$.

At a value of ν between 495 and 500 $\text{m}^2 \text{s}^{-1}$, the limit cycle experienced a subharmonic bifurcation, corresponding to a period-doubling instability (Drazin 1992). Period doubling in the wind-driven circulation was also observed in the models of MB1 and BM1.

The period-doubled limit cycle experienced a secondary Hopf bifurcation at a value of ν between 465 and 470 $\text{m}^2 \text{s}^{-1}$. The new frequency that appeared in the system due to the Hopf bifurcation was about 0.007 . . . rad/day (a period of roughly 900 days). We made this estimate from a quasiperiodic trajectory on the torus at 465 $\text{m}^2 \text{s}^{-1}$. We computed another stable torus with quasiperiodic motion on it at $\nu = 460 \text{ m}^2 \text{ s}^{-1}$.

We found chaotic attractors at $\nu = 450$ and 430 $\text{m}^2 \text{s}^{-1}$. It is not clear whether the chaotic attractor was preceded by a third Hopf bifurcation. The low-frequency end of the spectrum is very noisy, and we were not able to distinguish a leading spike, which might be associated with a third Hopf bifurcation. The branch of chaotic attractors exists down to $\nu = 340 \text{ m}^2 \text{ s}^{-1}$. When we used a point on a trajectory on the chaotic attractor at $\nu = 340 \text{ m}^2 \text{ s}^{-1}$ as the initial condition for the time integration at $\nu = 339 \text{ m}^2 \text{ s}^{-1}$, the resulting trajectory converged to a limit cycle (see the bifurcation diagram in Fig. 9). When we used a point on a trajectory on the limit cycle at $\nu = 339 \text{ m}^2 \text{ s}^{-1}$ as the initial condition for a run at $\nu = 340 \text{ m}^2 \text{ s}^{-1}$, the trajectory returned to the chaotic attractor. One possible explanation of such behavior may be the following. In the interval $339 \text{ m}^2 \text{ s}^{-1} < \nu < 340 \text{ m}^2 \text{ s}^{-1}$, the system experienced a pair of successive reverse Hopf bifurcations leading from the chaotic attractor to a torus and from the torus to a limit cycle. Either the range of ν for which the stable torus exists is very narrow or the torus may be unstable. The trajectory converged very slowly to a limit cycle at $\nu = 339 \text{ m}^2 \text{ s}^{-1}$. When we used a point on a trajectory on this limit cycle as the initial condition at $\nu = 340 \text{ m}^2 \text{ s}^{-1}$, for a long period of time the trajectory very slowly diverged from the unstable limit cycle as a tight spiral on the Poincaré section. This slow convergence and divergence at values of ν slightly lower and higher than the critical value supports the hypothesis of an intermediate reverse Hopf bifurcation from the limit cycle to a torus rather than the occurrence of phase locking.

The information dimension of the chaotic attractor at $\nu = 450 \text{ m}^2 \text{ s}^{-1}$ was estimated to be between 3.14 and 3.16. In order to estimate it, a time series of total energy of 10^5 points (each one is one day apart) was computed first and then extended up to 1.5×10^5 points. Both time series yielded the same estimate.

On the branch of predominantly chaotic attractors, we found four examples of phase locking (Arnold 1965; Drazin 1992). At $\nu = 440 \text{ m}^2 \text{ s}^{-1}$, phase locking between $\omega_1 = 0.068$. . . rad/day and $\omega_2 = 0.0068$. . . rad/day with ratio $\omega_2/\omega_1 = 1/10$ yielded a stable torus with quasiperiodic motion upon it. At $\nu = 420 \text{ m}^2 \text{ s}^{-1}$, phase locking between all frequencies led to a limit cycle with a period of 943 days and an amplitude somewhat less than the amplitudes of the neighboring chaotic attractors. At $\nu = 370 \text{ m}^2 \text{ s}^{-1}$, we found a torus with three dominant spectral spikes at 0.064 . . . , 0.0089 . . . , and 0.0039 . . . rad/day (periods are about 98, 710, and 1600 days, respectively). It is hard to say which of these three spikes correspond to the phase-locked frequencies. When we used a point on a trajectory belonging to the torus as an initial condition at $\nu = 375 \text{ m}^2 \text{ s}^{-1}$, the trajectory returned to the chaotic attractor. At $\nu = 365 \text{ m}^2 \text{ s}^{-1}$, phase locking between all frequencies led to a limit cycle with a period of 2060.5 days. In general, we expect this “chaotic region” of parameter space to have a very complicated structure. A complicated sequence of a chaotic attractors with embedded phase-locked tori and limit cycles was found in BM1, when R_d was used as the control parameter.

In the range of ν between 112 and 339 $\text{m}^2 \text{s}^{-1}$, the only stable attractors we found were tori and limit cycles. The

disappearance of the chaotic attractors suggests that the flow became “better” organized and contains a smaller number of active independent degrees of freedom. In the first set of experiments, we also encountered a similar organization of the flow expressed by the presence of the quasiperiodic branches surrounded by chaotic attractors. Note from Fig. 10 that, as ν is diminished, the mean energy of the attractors decreases more rapidly in this set of experiments than in the first set of experiments with less nonlinear circulation and larger R_d . In Fig. 11, we plotted the mean potential and kinetic energies of the attractors. The decrease of the total flow energy is due mainly to the decrease in the potential energy, which is associated with the time-dependent flow becoming more barotropic. The flow in the first set of experiments exhibited a similar decrease in the potential energy for diminishing ν .

What happens to the circulation? In Fig. 12 we show the time averages $\langle \psi_{1,2} \rangle$ of the limit cycles at $\nu = 338$ and 215 (the lower energy branch) and $115 \text{ m}^2 \text{ s}^{-1}$. As viscosity decreases, the time-averaged circulation of the upper layer develops a peripheral jet flowing along the walls in the western half of the basin. In the eastern half of the basin, the northern and southern parts of the jet are connected by a slow and wide current. In contrast to the second set of experiments, the upper-layer circulation in the first set had well-observed inertial recirculation gyres both in the time-averaged and instantaneous flows. The lower layer in the second set is dominated by a cyclonic circulation (similar to the lower-layer circulation in the first set of experiments) with one or two recirculation gyres in the western part of the basin outside a western boundary current. A weaker, anticyclonic recirculation in the lower layer occupies the northern part of the basin. The strength of the circulation in the lower layer increases as ν is reduced. This barotropization of the flow reduces the potential energy as was shown in Fig. 11.

A branch of simple attractors continued from $\nu = 339$ down to $\nu = 213 \text{ m}^2 \text{ s}^{-1}$. At the highest values of ν , these were limit cycles. For some value of ν between 300 and $310 \text{ m}^2 \text{ s}^{-1}$, the limit cycle lost stability via a Hopf bifurcation and the attractor became toroidal. The system returned to a limit cycle at a value of ν between 270 and $275 \text{ m}^2 \text{ s}^{-1}$, probably as a result of a supercritical reverse Hopf bifurcation. The second frequency on this branch of tori was about $0.018 \dots \text{ rad/day}$ (a period of 350 days). The branch of limit cycles became unstable and could not be followed by our methods below $\nu = 213 \text{ m}^2 \text{ s}^{-1}$. Another branch of stable limit cycles with smaller amplitude appeared at a value of ν slightly above $220 \text{ m}^2 \text{ s}^{-1}$. The spatial structures and frequencies of the flow on both limit cycles are similar. It is possible that this branch is a continuation of the higher amplitude branch and that there is an unstable branch connecting both stable branches, though we have not looked for unstable limit cycles. Multiple stable limit cycles coexist for ν between 213 and $220 \text{ m}^2 \text{ s}^{-1}$.

The new branch of limit cycles continued to lower ν . A Hopf bifurcation of the limit cycle occurred at ν between 182 and $185 \text{ m}^2 \text{ s}^{-1}$. The second frequency of motion on the torus generated was about $0.009 \dots \text{ rad/day}$ (a period of about 700 days). A reverse Hopf bifurcation at ν between 162 and $165 \text{ m}^2 \text{ s}^{-1}$ again yielded a limit cycle. The limit cycles either became unstable or ceased to exist at $\nu = 150 \text{ m}^2 \text{ s}^{-1}$. At $\nu = 150 \text{ m}^2 \text{ s}^{-1}$, the trajectory left the main branch of attractors and converged to a torus on a new branch of attractors denoted **A** on the bifurcation diagram.

Branch **A** overlaps with the main branch at $\nu = 151 \text{ m}^2 \text{ s}^{-1}$. Thus, there are two attractors at this value of viscosity: one is a limit cycle on the main branch and the other is a torus on branch **A**. For $100 \text{ m}^2 \text{ s}^{-1} \leq \nu \leq 135 \text{ m}^2 \text{ s}^{-1}$, there is a third branch of attractors, denoted **B** on the bifurcation diagram. The tori on branch **A** at ν equal to 150 and $151 \text{ m}^2 \text{ s}^{-1}$ have a second frequency of about $0.009 \dots \text{ rad/day}$ (a period of 700 days). At $\nu = 152 \text{ m}^2 \text{ s}^{-1}$, branch **A** either loses stability or ceases to exist, and the trajectory returns to a limit cycle on the main branch of stable attractors. At $\nu = 145 \text{ m}^2 \text{ s}^{-1}$ on branch **A** we found a limit cycle, which suggests another reverse Hopf bifurcation at ν between 145 and $150 \text{ m}^2 \text{ s}^{-1}$. The stable limit cycles on branch **A** continue to exist down to $\nu = 130 \text{ m}^2 \text{ s}^{-1}$. For somewhat lower viscosity, the limit cycle lost stability as a result of a Hopf bifurcation, and branch **A** continued to exist for lower viscosities as a family of tori. The second frequency of the tori is about $0.007 \dots \text{ rad/day}$ (a period of about 900 days). The tori lose stability at ν slightly less than $120 \text{ m}^2 \text{ s}^{-1}$.

We traced branch **B** (as it is denoted on the bifurcation diagram) of stable attractors, from $\nu = 135$ down to $\nu = 100 \text{ m}^2 \text{ s}^{-1}$. The attractors on this branch have stable neighboring attractors on branch **A** for values of ν between 120 and $135 \text{ m}^2 \text{ s}^{-1}$. On branch **B** we found limit cycles at $\nu = 115$ and $130 \text{ m}^2 \text{ s}^{-1}$. Hopf bifurcations occur at ν slightly less and higher than $130 \text{ m}^2 \text{ s}^{-1}$, connecting the limit cycle there with two families of tori. The family with higher ν either becomes unstable or ceases to exist at $\nu = 136 \text{ m}^2 \text{ s}^{-1}$ and the trajectory in that case is attracted to a limit cycle on branch **A**. The second frequency for this branch of tori is about $0.007 \dots \text{ rad/day}$ (a period of about 900 days). Another pair of Hopf bifurcations occur at ν slightly less and higher than $115 \text{ m}^2 \text{ s}^{-1}$. The family of tori that lies between 115 and $130 \text{ m}^2 \text{ s}^{-1}$ has a second frequency associated with motion on them of about $0.013 \dots \text{ rad/day}$ (a period of about 480 days). For $\nu < 115 \text{ m}^2 \text{ s}^{-1}$,

we computed a torus at $112 \text{ m}^2 \text{ s}^{-1}$ with a second frequency of about $0.009 \dots \text{ rad/day}$ (a period of about 700 days). This suggests the existence of a Hopf bifurcation at some value of ν between 112 and $115 \text{ m}^2 \text{ s}^{-1}$. For lower values of ν , we found only chaotic attractors at $\nu = 110$ and $100 \text{ m}^2 \text{ s}^{-1}$. The power in the low-frequency part of the chaotic spectra increases significantly as ν is reduced from 110 to $100 \text{ m}^2 \text{ s}^{-1}$. This result is consistent with the results of MB1 and BM1 that the low-frequency part of the spectrum dominates as the flow becomes more chaotic.

What happens to the perturbation fields $\psi'_{1,2}$, which were defined in (11) and (12), when the circulation develops a peripheral current? In Figs. 13a,b, we show the full upper- and lower-layer streamfunctions ψ_1 and ψ_2 for the limit cycle belonging to branch **B** at $\nu = 130 \text{ m}^2 \text{ s}^{-1}$. The period of this limit cycle is 109.6 days, which is much shorter than the period of the gravest basin mode. The upper-layer velocity is about 0.30 m s^{-1} at its maximum and the lower-layer velocity is about 0.05 m s^{-1} at its maximum. The perturbation fields $\psi'_{1,2}$ are shown in Figs. 14a,b. Note that the peripheral current includes a sequence of baroclinic eddies propagating cyclonically along the lateral walls of the basin. The quasiperiodic and chaotic behavior of the flow in the first set of experiments also contained baroclinic eddies, propagating cyclonically along the walls, but the amplitudes of these eddies were smaller than the amplitude of the time-averaged flow. The eddies in that case were weaker, the jet was weaker, and the velocity and pressure gradients near the walls were significantly less than in the second set of experiments.

For comparison with the limit cycle in Figs. 13a,b and 14a,b, we computed the equivalent-barotropic circulation for $\nu = 130 \text{ m}^2 \text{ s}^{-1}$ with all other parameters, except γ (in the equivalent-barotropic limit $\gamma \rightarrow 0$), the same as for the baroclinic limit cycle. The resulting circulation is steady and stable. It contains three recirculation gyres of unequal strength and is shown in Fig. 15. The striking difference between Fig. 15 and Figs. 13a,b and 14a,b emphasizes the crucial role of baroclinicity in determining both the mean circulation and the time-dependent dynamics of the flow, even when the ratio of layer depths γ is small.

The sizes and baroclinic structure of the eddies resemble those of the Black Sea eddies associated with the Rim Current (Oguz et al. 1993). Since the first baroclinic deformation radius of the Black Sea is similar to the value used here, this is, perhaps, not too surprising. The eddies in our simple model propagate freely along the walls, whereas in the Black Sea the eddies may be locked to topographic features, which we did not consider.

If the time-averaged circulation patterns at $\nu = 338$ and $215 \text{ m}^2 \text{ s}^{-1}$ (see Fig. 12) are compared, one can see that the recirculation gyres observed at all values of ν in the first set of experiments and at $\nu = 338 \text{ m}^2 \text{ s}^{-1}$ in the second set are scarcely evident at $\nu = 215 \text{ m}^2 \text{ s}^{-1}$. The disappearance of the gyres is associated with the development of the peripheral current as ν is reduced. In the upper layer the peripheral current, when well developed (as at $\nu = 215 \text{ m}^2 \text{ s}^{-1}$ and lower), flows around a single cyclonic cell occupying the whole basin. It is possible that this regime corresponds to the single-cell circulation in the Black Sea, which occurs when the gyres merge (Oguz et al. 1993).

4. Results: Primary instability


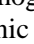
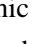
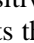
To investigate the physics behind the primary oscillatory instability, we used an approach based upon the energetics of the system. This approach was applied in previous studies (MB1, BM1) of barotropic and equivalent-barotropic wind-driven circulation and is as follows. For the most unstable eigenmode of a steady unstable fixed point, we computed the associated eddy-mean energy conversion terms, which are functions of the spatial variables. The spatial distributions and the signs of these terms allowed us to locate the regions that seem most active in supporting the instability of the circulation.

Because the instability is an oscillatory one, close to the stability threshold there are two distinct timescales, the (short) period of the oscillation and the long e -folding time. We can exploit this by integrating quantities over the period of the oscillatory instability. The resulting short-term averaged quantities are slowly varying on the long timescale. Denoting the slowly varying mean streamfunctions by $\Psi_{1,2}$, we can then define rapidly varying time-dependent perturbation

streamfunctions, $\psi'_{1,2} = \psi_{1,2} - \Psi_{1,2}$. By considering the slowly varying mean and perturbation energy equations in the usual way, we obtain slowly varying averages of the energy exchange terms between the slowly varying mean flow and the perturbation:

$$R = -\epsilon \frac{1}{(1 + \gamma)^2} \left\langle (\psi'_1 - \psi'_2) J \left(\frac{1}{2} [\psi'_1 + \psi'_2], \Psi_1 - \Psi_2 \right) \right\rangle. \quad (13)$$

The first term, P , is the energy exchange between the mean flow and the perturbations due to the rate of working of the Reynolds stresses. Positive P is characteristic of horizontal shear-flow instability. The second term, R , represents the energy exchange associated with the transport of interface height fluctuations. Positive R is characteristic of baroclinic instability. In those regions of the circulation where the sum of the exchange terms, $P + R$, is positive, perturbations gain energy from the basic state. We are interested in localizing these regions in order to identify the cause of the instability.

We computed the exchange terms for the unstable growing eigenmode of the unstable fixed point at $\nu = 220 \text{ m}^2 \text{ s}^{-1}$ (see the perturbation streamfunction plots in [Fig. 16](#) ) . The exchange terms are shown in [Fig. 17](#)  . First, the maxima and minima of P and R are concentrated in the western recirculation gyre; second, whereas the area integral of R over the basin has a positive value, the area integral of P is somewhat smaller and has a negative value. From the distribution and the signs of the energy conversion and, also, from the spatial structure of the eigenmode we conclude that the primary instability in the system is a baroclinic instability of the western gyre. This seems, from the perturbation streamfunction plots, to be similar to an azimuthal mode 2 instability of a baroclinic vortex ([Flierl 1988](#)) distorted by the basin boundaries and the flow beyond the recirculation gyre. The spatial inhomogeneity in the problem is reflected in the persistence of some of the wavelike structure in the time-averaged baroclinic conversion term ([Fig. 17](#) ). The energy conversion terms computed for the most unstable eigenmode of the unstable fixed point at $\nu = 550 \text{ m}^2 \text{ s}^{-1}$ and the depth ratio $\gamma = 1/19$ are shown in [Fig. 18](#)  . Once again, the area integral of R has a positive value, whereas the area integral of P has a negative value somewhat smaller than that of R . This result again suggests that baroclinic instability of the gyre is responsible for the primary instability in the system.

5. Discussion and conclusions

In this study we extended the results of MB1 and BM1 to a two-layer quasigeostrophic model of the wind-driven circulation in a closed basin. In analyzing the results of a standard numerical GCM, we treat it as a large-dimensional dynamical system with steady forcing and dissipation in the same way as in MB1 and BM1. In this paper, we introduce baroclinic physics into the model. The results of MB1 and BM1 suggested that for a wide range of the control parameters, the dynamics of the barotropic and the equivalent-barotropic models are strikingly low-dimensional. This means that in the large-time asymptotic limit, the phase space trajectory converges to low-dimensional objects such as fixed points, limit cycles, tori, and strange attractors. As the control parameters are changed, these simple invariant sets may become unstable or disappear as a result of bifurcations in the dynamical system. This low-dimensional dynamics and the corresponding time-dependent behavior are intrinsic properties of the system based upon the nonlinearity of the equations and internal instabilities of the solutions. Theoretical reasons for why low-dimensional attractors should exist in an oceanic primitive-equations model are discussed in [Lions et al. \(1992\)](#). Low-dimensional behavior has also been found in oceanic models by [Jiang et al. \(1995\)](#), [Speich et al. \(1995\)](#), [Kamenkovich et al. \(1995\)](#), and [Sheremet et al. \(1995\)](#).

An important question is how robust is this low-dimensionality? How does it depend upon the physics involved in the model? Does it exist in modern sophisticated general circulation models? In this study we introduced the simplest two-layer baroclinicity in the model, and the results suggested that low-dimensionality was preserved for a wide range of viscosity coefficient, which was the main variable control parameter. This is our central result. The complexity and dimensionality of the attractors found tend to increase as the dissipation is reduced. Low-dimensional dynamics should be present in any dissipative GCM driven by nonstochastic forcing in the absence of discontinuous processes such as “convective adjustment.” In general, the location of these attractors and the nature of the bifurcations in the model will depend on the physical processes included in the model.

The types of low-dimensional behavior of the wind-driven circulation seen in this baroclinic study resemble those seen in the barotropic study of MB1 and the reduced gravity model of BM1. We anticipate that the sensitivity to discretization will also be similar to that seen in MB1 and BM1. The main differences seen as resolution was increased in the latter two works were that the bifurcation thresholds shifted slightly while the amplitudes and timescales of the time-dependent solutions change by a few percent. This suggests that in the 2LQG case, as in the barotropic and equivalent barotropic cases, the details of the bifurcation sequences may change slightly as the resolution is increased, but the wide range of low-dimensionality will be robust and the route to chaos will not change. (The locations of episodes of phase locking within the chaotic regime are likely to change.) However, given the smaller scale of the deformation radius in the second set of experiments described in the present paper ($R_d = 16.813 \text{ km}$) compared to the deformation radius in the first set ($R_d = 23.148 \text{ km}$) and in the EB case ($R_d = 24.4 \text{ km}$), we expect the second set to exhibit larger sensitivity. This is borne out by experiments with the 2LQG model at enhanced resolution. As an example, the case $\gamma = 1/9$, $R_d = 23.148 \text{ km}$, $\nu = 200 \text{ m}^2 \text{ s}^{-1}$, at 6.25-km resolution yields a limit cycle with an energy amplitude equal to 2.7% of the mean energy and a period of

about 115 days. At a resolution of 3.125 km, we again see a limit cycle but the period has shifted to about 112 days, while the amplitude is 2.6% of the mean energy. With the shorter deformation radius, larger changes are seen; a run with $\gamma = 1/19$, $R_d = 16.813$ km, $\nu = 520$ m² s⁻¹, and 6.25-km resolution yields a limit cycle with an amplitude equal to 0.6% of the mean and a period of 91.5 days, while at 3.125-km resolution, the amplitude increases to 1.2% and the period becomes 93.5 days.

As the control parameters are varied, the topology of the attractors changes due to successive bifurcations. We found that the most common route from a fixed point to a strange attractor in these single-gyre models, whether barotropic, equivalent barotropic, or baroclinic, consists of three successive Hopf bifurcations: from a fixed point to a limit cycle, from a limit cycle to a torus, and from a torus to a strange attractor. For some values of the control parameters we found an intermediate period-doubling bifurcation of a limit cycle. Similar period doublings were found in the oceanic models of MB1 and BM1. These results suggest that while period doublings may not be uncommon in ocean GCMs, an infinite succession of period doublings (cf. [Feigenbaum 1978, 1979](#)) is unlikely and the main route to chaos should involve successive Hopf bifurcations. This is a Ruelle–Takens route to chaos (suggested by [Ruelle and Takens 1971](#)). For discussion of the Ruelle–Takens scenario see [Newhouse et al. \(1978\)](#) and [Eckmann \(1981\)](#).

We showed that the low-dimensional dynamics introduces low-frequency variability of the flow. This variability is important for long-term predictions or climate studies. In the results reported here, secondary frequencies on some tori yielded interannual and decadal variability of the flow. Interdecadal variability was associated with motion on strange attractors. As the complexity of strange attractors grows, the spectral power at low frequencies grows disproportionately. This behavior was observed in MB1 and BM1 and is, presumably, typical for wind-driven circulation models. This climatological variability in the baroclinic model, as well as the variability in the models discussed in MB1 and BM1, arises in the flow without any long-term fluctuations in the external forcing. It is due to intrinsic instabilities and the nonlinearity of the circulation. At the present time there are several explanations of long-term variability in the midlatitude ocean driven by atmospheric forcing. [Hasselmann \(1976\)](#) proposed a model in which stochastic forcing of the ocean by the atmosphere at all frequencies drives a low-frequency response. In that case, the spectrum associated with the variability of the ocean has a broad band at low frequencies with no spectral peaks. [James and James \(1989\)](#) showed that the atmosphere itself may possess low-frequency intrinsic variability when forced only with the annual cycle. This variability may cause the ocean's response on the same timescales. Oscillations of the midlatitude ocean–atmosphere system coupled through wind forcing and thermodynamic processes were found in the numerical study of [Latif and Barnett \(1994\)](#). They found a coupled decadal oscillatory mode in the North Pacific Ocean. In addition to these scenarios for the low-frequency variability in the midlatitude ocean, our present study, as well as the MB1, BM1, [Jiang et al. \(1995\)](#) and [Speich et al. \(1995\)](#) results, adds one more scenario. Namely, it suggests that natural variability (i.e., free from variations in external forcing) of the midlatitude ocean may occur on climatological timescales.

The question of how natural climatological variability will be affected by temporal variations in the forcing is still open. An understanding of low-dimensional dynamics may be important in answering it. We expect that, in some regimes, the flow driven by a stochastic time-dependent forcing will have a tendency to stay longer in the vicinity of the attractors of the same system driven by a steady forcing “close” to the time-dependent forcing, for example, a time average of the unsteady forcing. In that case the attractors will be associated with the most statistically probable states of the flow. When the forcing is simply periodic, the forcing can be incorporated in the framework described above by formally adding a pair of extra variables whose evolution equations reproduce the time-dependent component of the forcing, converting the nonautonomous problem into an autonomous one. The additional variables are not dissipated in the same way as the original variables. In the limit of strong dissipation, these variables continue to oscillate and so the strong dissipation limit is a limit cycle rather than a fixed point. One advantage of adopting this point of view is that it provides a unifying perspective that can include both the work described above and results from models of El Niño of the sort described in [Jin et al. \(1994\)](#) and [Tziperman et al. \(1994\)](#). Whether the route to chaos will then be via overlapping resonances on a torus as in the latter two references or one of the other routes to chaos from a torus remains to be seen.

A useful comparison can be made between the baroclinic model circulation and the observations of flow patterns in the Black Sea. The Black Sea exhibits the interesting phenomenon of large-scale organization. The circulation in the Black Sea is predominantly cyclonic. A prominent feature of this circulation is a recurrent appearance of two cyclonic cells (the Western and Eastern Gyres)—one in the eastern and the other in the western part of the basin. At other times the upper-layer flow is dominated by a basin wide Rim Current, and the gyres are less prominent. The barotropic and equivalent-barotropic models used in MB1 and BM1 were able to reproduce two cyclonic recirculations, which are analogous to those observed in the Black Sea, for a wide range of ν and R_d . In the baroclinic case, the gyres were observed for all values of ν in the first set of experiments, when the layer depths were $H_1 = 200$ m and $H_2 = 1800$ m. In the second set of experiments with $H_1 = 100$ m and $H_2 = 1900$ m the gyres disappeared gradually when ν was reduced. This process was associated with the developing of a peripheral cyclonic current in the western half of the basin. In the eastern part of the basin the current was rather slow and wide. The current was essentially baroclinic. It was filled with a “chain” of baroclinic eddies associated with vigorous meandering of the main jet. The eddies propagated cyclonically along the basin's walls. We found that this seemingly complicated behavior might be achieved on relatively simple dynamical attractors such as limit cycles and tori. The observations of the Black Sea circulation ([Oguz et al. 1993](#)) showed a cyclonic Rim Current filled with baroclinic eddies. It

is possible that the peripheral current in the model may be analogous to the Rim Current. No peripheral current was found in the barotropic and equivalent-barotropic models of MB1 and BM1. This suggests that the nature of the peripheral current is essentially baroclinic, which accords with observations (Filippov 1961; Oguz et al. 1993). In our experiments we obtained a transition between gyre-dominated flows and Rim Current-dominated flows by varying the stratification. In the real Black Sea, such transitions are likely to depend on seasonal fluctuations in the strength of the wind as well as on the seasonal variations in the pycnocline due to surface heat and freshwater fluxes. It would be interesting to continue this work by adding a simple seasonal cycle to the wind forcing.

We examined the nature of the primary instability of the flow and found that the onset of oscillatory instability occurs as a result of baroclinic instability in the western recirculation gyre. The comparison of this instability with the complicated shear-flow instability seen in the equivalent-barotropic model (see BM1) involving the western boundary intensification, the western gyre, and the meander between the western and central gyres, and the similarly complicated shear-flow instability of the barotropic circulation (Meacham and Berloff 1996b) emphasizes the important role of baroclinicity in time-dependent general circulation problems (cf. Holland 1978).

Last, we note a feature common to barotropic, equivalent-barotropic, and baroclinic models of the wind-driven circulation: the existence of parameter regimes in which multiple, stable, time-dependent regimes coexist.

Acknowledgments

This work was supported by the National Science Foundation (Grant OCE-9301318). We are grateful to E. Kostelich for the numerical code for the fractal dimension estimate and to several of our colleagues for opportunities to discuss various aspects of the general circulation.

REFERENCES

- Arnold, V., 1965: *Small Denominators*. Vol. I, *Mappings of the Circumference onto Itself*. Amer. Math. Soc. Transl. Ser. 2, **46**, 213–284..
- Badii, R., and A. Politi, 1985: Statistical description of chaotic attractors: The dimension function. *J. Stat. Phys.*, **40**, 725–750..
- Bak, P., T. Bohr, and M. H. Jensen, 1985: Mode-locking and the transition to chaos in dissipative systems. *Physica Scripta*, **9T**, 50–58..
- Battellino, P., C. Grebogi, E. Ott, and J. Yorke, 1989: Chaotic attractors on an 3-torus, and the torus break-up. *Physica D*, **39**, 299–314..
- Berloff, P. S., and S. P. Meacham, 1997: The dynamics of an equivalent-barotropic model of the wind-driven circulation. *J. Mar. Res.*, **55**, 407–451..
- Brandstater, A., and H. L. Swinney, 1987: Strange attractors in weakly turbulent Couette–Taylor flow. *Phys. Rev.*, **35 A**, 2207–2220..
- Broomhead, D., and G. King. 1986: Extracting qualitative dynamics from experimental data. *Physica D*, **20**, 217–236..
- Bryan, K., 1963: A numerical investigation of a nonlinear model of a wind-driven ocean. *J. Atmos. Sci.*, **20**, 594–606.. [Find this article online](#)
- Cessi, P., and G. Ierley, 1995: Symmetry-breaking multiple equilibria in quasigeostrophic wind-driven flows. *J. Phys. Oceanogr.*, **25**, 1196–1205..
- Collet, P., and J.-P. Eckmann, 1980: *Iterated Maps on the Interval as Dynamical Systems*. Birkhäuser, 248 pp..
- Constantin, P., C. Foias, B. Nicolaenko, and R. Temam, 1989: *Integral Manifolds and Inertial Manifolds for Dissipative Partial Differential Equations*. Springer-Verlag, 122 pp..
- Drazin, P., 1992: *Nonlinear Systems*. Cambridge University Press, 317 pp..
- Eckmann, J.-P., 1981: Roads to turbulence in dissipative dynamical systems. *Reviews of Modern Phys.*, **53**, 643–654..
- Farmer, J., E. Ott, and J. Yorke, 1983: The dimension of chaotic attractors. *Physica D*, **7**, 153–180..
- Feigenbaum, M., 1978: Quantitative universality for a class of non-linear transformations. *J. Stat. Phys.*, **19**, 25–52..
- , 1979: The universal metric properties of non-linear transformations. *J. Stat. Phys.*, **21**, 669–706..

Fein, A. P., M. S. Heutmacher, and J. P. Gollub, 1985: Scaling at the transition from quasiperiodicity to chaos in a hydrodynamic system. *Physica Scripta*, **9T**, 79–84..

Filippov, D., 1961: On the abyssal horizontal circulation of the Black Sea. *Proc. Oceanogr. Inst.*, **53**, 112–122..

Flierl, G., 1988: On the instability of geostrophic vortices. *J. Fluid Mech.*, **197**, 349–388..

Fofonoff, N., 1954: Steady flow in a frictionless homogeneous ocean. *J. Mar. Res.*, **13**, 254–262..

Franceschini, V., and C. Tebaldi, 1984: Breaking and disappearance of tori. *Commun. Math. Phys.*, **94**, 317–329..

Giberti, C., and R. Zanasi, 1993: Behavior of a three-torus in truncated Navier–Stokes equations. *Physica D*, **65**, 300–312..

Gollub, J., and S. Benson, 1980: Many routes to turbulent convection. *J. Fluid Mech.*, **100**, 449–470..

Hasselmann, K., 1976: Stochastic climate models. Part I. Theory. *Tellus*, **28**, 473–485..

Holland, W., 1978: The role of mesoscale eddies in the general circulation of the ocean—Numerical experiments using a wind-driven quasigeostrophic model. *J. Phys. Oceanogr.*, **8**, 363–392..

Ierley, G. R. and W. R. Young, 1991: Viscous instabilities in the western boundary layer. *J. Phys. Oceanogr.*, **21**, 1323–1332..

—, and V. Sheremet, 1995: Multiple solutions and advection-dominated flows in the wind-driven circulation. Part I: Slip. *J. Mar. Res.*, **53**, 703–737..

James, I., and P. James, 1989: Ultra-low-frequency variability in a simple atmospheric circulation model. *Nature*, **342**, 53–55..

Jiang, S., F. Jin, and M. Ghil, 1995: Multiple equilibria, periodic, and aperiodic solutions in a wind-driven, double-gyre shallow-water model. *J. Phys. Oceanogr.*, **25**, 764–786..

Jin, F.-F., J. D. Neelin, and M. Ghil, 1994: El Nino on the Devil’s staircase: Annual subharmonic steps to chaos. *Science*, **264**, 70–72..

Kamenkovich, V., V. Sheremet, A. Pastushkov, and S. Belotserkovsky, 1995: Analysis of the barotropic model of the subtropical gyre in the ocean for finite Reynolds numbers. Part I. *J. Mar. Res.*, **53**, 959–994..

Kostelich, E. J., 1990: Software for calculating attractor dimension using the nearest neighbor algorithm with accompanying text. [Available at eric@chaos.utexas.edu.]

Latif, M., and T. Barnett, 1994: Causes of decadal climate variability over the North Pacific and North America. *Science*, **266**, 634–637..

Lions, J.-L., R. Temam, and S. Wang, 1992: On the equations of the large-scale ocean. *Nonlinearity*, **5**, 1007–1053..

McCalpin, J. and D. Haidvogel, 1996: Phenomenology of the low-frequency variability in a reduced-gravity, quasigeostrophic double-gyre model. *J. Phys. Oceanogr.*, **26**, 739–752..

Meacham, S. P., and P. Berloff, 1997: Barotropic wind-driven circulation in a small basin. *J. Mar. Res.*, **55**, 523–563..

Moore, D. W., 1963: Rossby waves in ocean circulation. *Deep-Sea Res.*, **10**, 735–748..

Newhouse, S., D. Ruelle, and F. Takens, 1978: Occurrence of strange axiom A attractors near quasi periodic flows on T^m , $m \geq 3$. *Commun. Math. Phys.*, **64**, 35–40..

Oguz, T., P. La Violette, and U. Unluata, 1992: The upper layer circulation of the Black Sea: Its variability as inferred from hydrographic and satellite observations. *J. Geophys. Res.*, **97**, 12569–12584..

—, V. Latun, M. Latiff, V. Vladimirov, H. Sur, A. Markov, E. Ozsoy, B. Kotovshchikov, V. Eremeev, and U. Unluata, 1993: Circulation in the surface and intermediate layers of the Black Sea. *Deep-Sea Res.*, **40**, 1597–1612..

Packard, N. H., J. D. Crutchfield, J. D. Farmer, and R. S. Shaw, 1980: Geometry from a time series. *Phys. Rev. Lett.*, **45**, 712–716..

Pedlosky, J., 1987: *Geophysical Fluid Dynamics*. 2d ed. Springer-Verlag, 710 pp..

Pfister, G., Th. Buzug, and N. Enge, 1992: Characterization of experimental time series from Taylor–Couette flow. *Physica D*, **58**, 441–454..

Phillips, N., 1954: Energy transformations and meridional circulations associated with simple baroclinic waves in a two-level, quasigeostrophic model. *Tellus*, **6**, 273–286..

Quon, S., and M. Ghil, 1996: Multiple equilibria and stable oscillations in thermosolutal convection at small aspect ratio. *J. Fluid Mech.*, **291**, 33–56..

Rhines, P., 1977: The dynamics of unsteady ocean currents. *The Sea*, E. D. Goldberg, I. N. McCave, J. J. O'Brien, and J. H. Steele, Eds., Vol. 6, Wiley, 189–318..

Robinson, J., 1995: Finite-dimensional behavior in dissipative partial differential equations. *Chaos*, **5**, 330–345..

Ruelle, D., and F. Takens, 1971: On the nature of turbulence. *Commun. Math. Phys.*, **20**, 167–192..

Sheremet, V., V. Kamenkovich, and A. Pastushkov, 1995: Analysis of the barotropic model of the subtropical gyre in the ocean for finite Reynolds numbers. Part II. *J. Mar. Res.*, **53**, 995–1024..

—, G. Ierley, and V. Kamenkovich, 1997: Eigenanalysis of the two-dimensional wind-driven ocean circulation problem. *J. Mar. Res.*, **55**, 57–92..

Speich, S., H. Dijkstra, and M. Ghil, 1995: Successive bifurcations in a shallow-water model applied to the wind-driven ocean circulation. *Nonlinear Proc. Geophys.*, **2**, 241–268..

Stanev, E. V., 1990: On the mechanisms of the Black Sea circulation. *Earth–Sci. Rev.* **28**, 285–319..

Takens, F., 1981: Detecting strange attractors in turbulence, *Dynamical Systems and Turbulence, Lecture Notes in Mathematics*, D. A. Rand, and L.-S. Young, Eds., Springer-Verlag, 361–381..

Temam, R., 1995: *Navier-Stokes Equations and Nonlinear Functional Analysis*. 2d ed., CBMS-NSF Regional Conference Series in Applied Mathematics, SIAM, 141 pp..

Tziperman, E., L. Stone, M. Cane, and H. Jarosh, 1994: El Nino chaos: Overlapping of resonances between the seasonal cycle and the Pacific ocean–atmosphere oscillator. *Science*, **264**, 72–74..

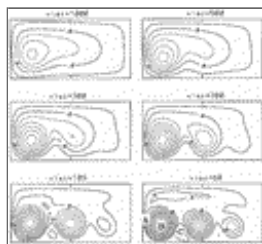
Tables

Table 1. Model parameters.

L_x	800 km (zonal basin width)
L_y	400 km (meridional basin width)
f_0	$.93 \times 10^{-4} \text{ s}^{-1}$ (planetary vorticity)
β_0	$2 \times 10^{-11} \text{ m}^{-1} \text{ s}^{-1}$ (planetary vorticity gradient)
g'	$2.575 \times 10^{-2} \text{ m s}^{-2}$ (reduced gravity)
τ_0	0.5 dyn/cm ² (wind stress)
H	2 km (total depth)
First set of experiments: $H_1 = 200 \text{ m}$, $H_2 = 1800 \text{ m}$, $R_2 = 23.148 \text{ km}$, $140 \text{ m}^2 \text{ s}^{-1} < \nu < 260 \text{ m}^2 \text{ s}^{-1}$	
Second set of experiments: $H_1 = 100 \text{ m}$, $H_2 = 1900 \text{ m}$, $R_2 = 16.813 \text{ km}$, $100 \text{ m}^2 \text{ s}^{-1} < \nu < 580 \text{ m}^2 \text{ s}^{-1}$	

[Click on thumbnail for full-sized image.](#)

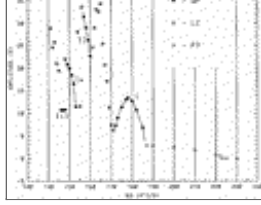
Figures



[Click on thumbnail for full-sized image.](#)

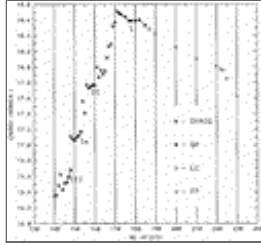
Fig. 1. From Berloff and Meacham (1997). The upper-layer streamfunction plots of six different steady solutions at the values of $\nu = 1000, 500, 300, 200, 105, 60 \text{ m}^2 \text{ s}^{-1}$. The lower layer is at rest and may have any depth. The upper-layer depth of these solutions is 200 m. On the last panel the following circulation features are noted: A—the western boundary intensification, which contains fluid from the interior of the basin and from the western recirculation gyre; B—the western recirculation gyre; C—the meander between the western and the central gyres.





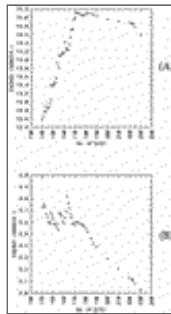
[Click on thumbnail for full-sized image.](#)

Fig. 2. Bifurcation diagram for $R_d = 23.148$ km. The oscillation amplitude as a percentage of mean amplitude versus ν . FP: fixed points; LC: limit cycles; QP: quasiperiodic motion on tori. The different branches of stable tori are denoted by I, Ia, II, and III.



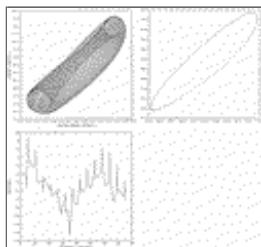
[Click on thumbnail for full-sized image.](#)

Fig. 3. The mean nondimensional energies of the attractors versus ν for $R_d = 23.148$ km, $\gamma = 1/9$. Note that, over part of the range of ν , the mean energy has a tendency to decrease as ν is reduced. FP: fixed points; LC: limit cycles; QP: quasiperiodic motion on tori.



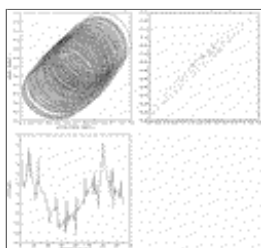
[Click on thumbnail for full-sized image.](#)

Fig. 4. (a) The mean potential energies of the attractors in the first set of experiments; (b) The mean kinetic energies of the attractors in the first set of experiments.



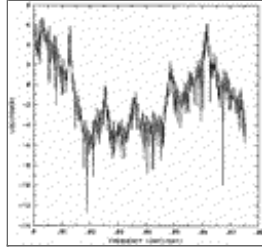
[Click on thumbnail for full-sized image.](#)

Fig. 5. Trajectory on the toroidal attractor at $\nu = 178 \text{ m}^2 \text{ s}^{-1}$ for $R_d = 23.148$ km, $\gamma = 1/9$. (a: top left) The delay coordinate phase space projection of the trajectory; (b: top right) Poincaré section of the trajectory; and (c: lower left) power spectrum of the time series corresponding to the trajectory. Note two dominant frequencies at $0.0055 \dots$ and $0.058 \dots$ rad/day (periods are near 1140 and 108 days, respectively).



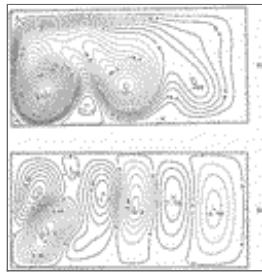
[Click on thumbnail for full-sized image.](#)

Fig. 6. Trajectory on the chaotic attractor at $\nu = 171 \text{ m}^2 \text{ s}^{-1}$ for $R_d = 23.148 \text{ km}$, $\gamma = 1/9$. (a) The delay coordinate phase space projection of the trajectory; (b) Poincaré section of the trajectory; and (c) power spectrum of the time series corresponding to the trajectory. Note the noisy structure of the spectrum. The dominant frequencies are approximately $0.06 \dots$, $0.013 \dots$, and $0.0057 \dots$ rad/day (the periods are about 480, 105, and 1100 days respectively).



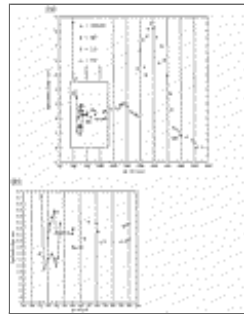
[Click on thumbnail for full-sized image.](#)

Fig. 7. Power spectrum of the time series corresponding to the trajectory on the chaotic attractor at $\nu = 167 \text{ m}^2 \text{ s}^{-1}$. Note that the power is concentrated mainly at the low-frequency end of the spectrum. This behavior is typical for the chaotic attractors found in the present study and the studies of MB1 and BM1.



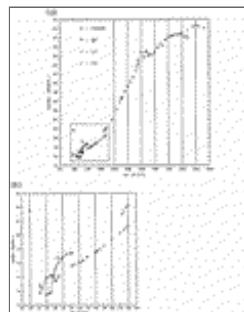
[Click on thumbnail for full-sized image.](#)

Fig. 8. Snapshots of the chaotic circulation at $\nu = 140 \text{ m}^2 \text{ s}^{-1}$ for $R_d = 23.148 \text{ km}$. The upper layer contains a pair of recirculation gyres (there is also a very weak recirculation in the eastern part of the basin), which show some similarity to the Western and Eastern Gyres in the Black Sea. (a) Ψ_1 (CI = 10), (b) Ψ_2 (CI = 2).



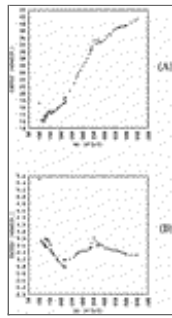
[Click on thumbnail for full-sized image.](#)

Fig. 9. (a) Bifurcation diagram for $R_d = 16.813 \text{ km}$. The square root of oscillation amplitude as a percentage of mean amplitude versus ν . FP: fixed points, LC: limit cycles, QP: quasiperiodic motion on tori. By PD we denoted the period doubling of the limit cycle. Two branches of attractors at low ν are denoted by **A** and **B**. (b) Enlargement of region in the box in (a).



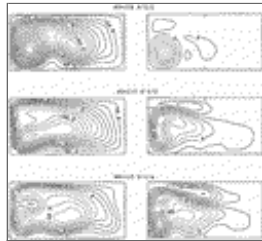
[Click on thumbnail for full-sized image.](#)

Fig. 10. (a) The mean nondimensional energies of the attractors found in the second set of experiments versus ν for $R_d = 16.813$ km. The mean energy decreases significantly as ν is reduced FP: fixed points, LC: limit cycles, QP: quasiperiodic motion on tori, PD: period doubling. (b) Enlargement of region in the box in (a).



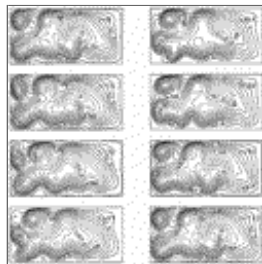
[Click on thumbnail for full-sized image.](#)

Fig. 11. (a) The mean potential energies of the attractors in the second set of experiments; (b) the mean kinetic energies of the attractors in the second set of experiments.



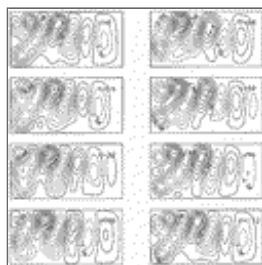
[Click on thumbnail for full-sized image.](#)

Fig. 12. The time averages $\langle \psi_{1,2} \rangle$ of the limit cycles at $\nu = 338, 215$ (the lower energy branch), and $115 \text{ m}^2 \text{ s}^{-1}$. The upper-layer streamfunctions $\langle \psi_1 \rangle$ are shown on the left panels, and the lower-layer streamfunctions $\langle \psi_2 \rangle$ are shown on the right panels. Note that with decreasing ν , the time-averaged upper-layer circulation develops a peripheral current.



[Click on thumbnail for full-sized image.](#)

Fig. 13. Time-dependent behavior of the streamfunctions $\psi_{1,2}$ on the limit cycle at $\nu = 130 \text{ m}^2 \text{ s}^{-1}$ over one period. Time t is measured in days. (a) The upper layer (CI = 15); (b) the lower layer (CI = 5).



[Click on thumbnail for full-sized image.](#)

Fig. 13. (Continued)





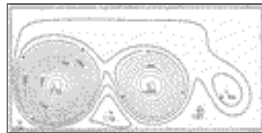
[Click on thumbnail for full-sized image.](#)

Fig. 14. Time-dependent behavior of the perturbation streamfunctions $\psi_{1,2}$ on the limit cycle at $\nu = 130 \text{ m}^2 \text{ s}^{-1}$ over one period. Time t is measured in days. Note the sequence of the baroclinic eddies propagating cyclonically along the lateral walls of the basin. (a) The upper layer (CI = 15); (b) the lower layer (CI = 5).



[Click on thumbnail for full-sized image.](#)

Fig. 14. (Continued)



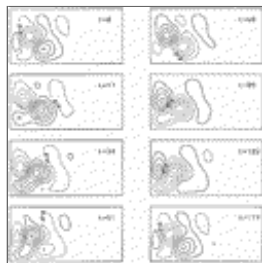
[Click on thumbnail for full-sized image.](#)

Fig. 15. The equivalent-barotropic streamfunction for $\nu = 130 \text{ m}^2 \text{ s}^{-1}$, $R_d = 16.813 \text{ km}$, and $H_1 = 100 \text{ m}$. The circulation is steady and stable. Note that the peripheral current does not develop in this case and the flow pattern is dominated by the main inertial recirculation gyres.



[Click on thumbnail for full-sized image.](#)

Fig. 16. Time-dependent behavior of the perturbation streamfunctions of the most unstable eigenmode at $\nu = 220 \text{ m}^2 \text{ s}^{-1}$ and $R_d = 23.148 \text{ km}$ over one eigenperiod. Time t is measured in days. (a) The upper layer; (b) the lower layer.



[Click on thumbnail for full-sized image.](#)

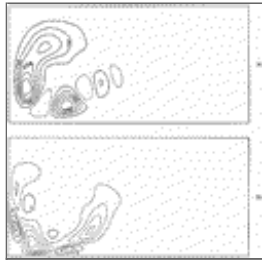
Fig. 16. (Continued)





[Click on thumbnail for full-sized image.](#)

Fig. 17. Spatial distribution of the energy conversion terms R and P corresponding to the most unstable growing eigenmode at $\nu = 220 \text{ m}^2 \text{ s}^{-1}$ and $R_d = 23.148 \text{ km}$. (a) R , (b) P .



[Click on thumbnail for full-sized image.](#)

Fig. 18. Spatial distribution of the energy conversion terms R and P corresponding to the most unstable growing eigenmode at $\nu = 550 \text{ m}^2 \text{ s}^{-1}$ and $R_d = 16.813 \text{ km}$. (a) R , (b) P .

Corresponding author address: S. P. Meacham, Department of Oceanography, The Florida State University, Tallahassee, FL 32306-3048.

E-mail: meach@tri.ocean.fsu.edu

[top ▲](#)



© 2008 American Meteorological Society [Privacy Policy and Disclaimer](#)
Headquarters: 45 Beacon Street Boston, MA 02108-3693
DC Office: 1120 G Street, NW, Suite 800 Washington DC, 20005-3826
amsinfo@ametsoc.org Phone: 617-227-2425 Fax: 617-742-8718
[Allen Press, Inc.](#) assists in the online publication of *AMS* journals.